A Second Order Accuracy Preserving Method for Moving Contact Line Problems

Shuqing Chai[a,b], Zhen Zhang[a,*], Zhiwen Zhang[b]

[a]*Department of Mathematics,*
Guangdong Provincial Key Laboratory of Computational Science and Material Design,
Southern University of Science and Technology (SUSTech), Shenzhen 518055, P.R.
China.
[b]*Department of Mathematics, The University of Hong Kong, Pokfulam Road, Hong Kong*
SAR.

Abstract

The immersed interface method (IIM) has been widely used in simulations of multiphase flows with closed interfaces. We generalize IIM to simulate the moving contact line (MCL) problems, which are modelled by the Stokes equation with Navier-slip boundary condition and the contact angle condition. With the help of variational formulation, the contact angle condition can be combined with the interfacial kinematics in a weak form. A parametric finite element method (PFEM) is applied to solve for the interface motion as well as the curvature, which are in turn used to update the correction terms for the irregular points in IIM. The hybrid IIM-PFEM method achieves second order accuracy not only in the velocity field, but also in the interface and the contact line motion. This is validated by numerical results. Moreover, we generalize the method to account for discontinuous viscosity. Various numerical experiments are presented in the study of droplet motion and contact angle hysteresis (CAH).

Keywords:
moving contact lines, contact angle hysteresis, immersed interface method, parametric finite element method

---

[*]Corresponding author. Address: Department of Mathematics, Southern University of Science and Technology (SUSTech), Shenzhen 518055, P.R. China.

Email addresses: `chaisq@mail.sustech.edu.cn` (Shuqing Chai), `zhangz@sustech.edu.cn` (Zhen Zhang), `zhangzw@hku.hk` (Zhiwen Zhang)

1. Introduction

When one fluid displaces another fluid on a solid substrate, a moving contact line is formed as the intersection of the fluid-fluid interface and the solid surface. Moving contact lines are widely observed in the nature and play very important roles in many physical phenomena, e.g., droplet wetting and dewetting, coffee ring effect, and contact angle hysteresis. Investigation of the contact line dynamics is helpful in promoting many industrial processes such as coating and inkjet printing [1, 2]. In the equilibrium state, the contact angle θ_y (or Young's angle) between the fluid-fluid interface and the solid surface is described by the Young's equation [3]:

$$\gamma \cos \theta_y = \gamma_2 - \gamma_1. \tag{1}$$

where $\gamma_i (i = 1, 2)$ and γ are the surface tensions of the two fluid-solid interfaces and the fluid-fluid interface respectively. The mismatch of the forces in this equation can lead to an unbalanced Young's stress in the dynamic process of moving contact lines. A difficulty arises when modelling moving contact lines using the classical hydrodynamics with the no-slip boundary condition: the stress has a non-physical singularity at the contact line with an infinite rate of energy dissipation. This is the well known contact line singularity [4, 5].

A large variety of models have been proposed to resolve this issue. These include kinetic models, molecular dynamics models, hydrodynamic models and diffuse-interface models [6, 7, 8, 9, 10, 11, 12, 13, 14]. In this work, we will follow the Navier slip model associated with the contact angle condition proposed by [15, 16]. This model was derived in a variational framework and shown to be thermodynamically consistent. We will make use of this variational structure to design an efficient numerical scheme in simulating contact line dynamics.

Simulations of multiphase flows are free boundary problems, which are in general difficult due to the moving interfaces and the coupling between the bulk equations and the interfacial conditions. A great number of numerical methods were proposed to consistently track the moving interfaces and solve for the coupling. Among them the most popular methods are volume of fluid method, level set method, front-tracking method, boundary integral method, immersed boundary method and immersed interface method [17, 18, 19, 20, 21, 22, 23, 24].

First proposed by Peskin [25], the immersed boundary (IB) method has been widely used in simulating interface problems. In IB method, the interface conditions are reformulated as singular forces in the whole domain with the help of Dirac delta functions. As a result, the bulk equations and the boundary conditions are combined in a unified Eulerian form, and can be solved on a uniform Cartesian grid. To numerically smooth out the singular forces on the interfaces, discrete delta functions are introduced to spread the interfacial forces from Lagrangian markers to Eulerian grid points. When the velocity field is solved, the same discrete function is applied to interpolate velocity field back to the Lagrangian markers on the interfaces and then the interfaces are updated using this velocity field. The IB method is easy to implement but yields only first-order accuracy. Moreover, the artificial parameter introduced in the discrete delta function may smear the accuracy in some circumstances such as contact line dynamics on rough surfaces. To avoid artificial parameters and improve the accuracy to second order, LeVeque and Li [26] introduced the immersed interface method (IIM) within the finite difference framework. The key idea lies in the use of jump conditions and the derivation of appropriate schemes on the irregular grid points near the interface. After the introduction of correction terms, the interfacial forces are immersed through the jump conditions in the Taylor expansion at the interfacial points [27]. Although IIM has been widely used in many interface problems, most works focused on closed interfaces while few studies investigated MCL problems with open interfaces [28].

In MCL problems, the contact line motion is driven by the unbalanced Young's stress while the interface motion is driven by the interior velocity field. Usually, the contact line dynamics is of the most interest, in particular in the study of contact angle hysteresis (CAH) on rough substrate. CAH describes the difference between the advancing and receding contact angles when a droplet moves along a microscopically rough solid surface in different directions. Numerical study of the detailed structure of CAH requires the very accurate tracking of the contact lines on the substrate with small scale roughness. Moreover, the accurate resolution of the velocity field heavily relies on the accurate approximation of interfacial geometries such as curvature and its derivatives. This is difficult in the moving contact line problems, where the redistribution of the interfacial markers is usually necessary and brings in errors in approximating the curvature. In this situation, a numerical scheme that resolves the velocity field and captures both interface and contact line motions with high order accuracy is in great demand.

3

Recently the parametric finite element method (PFEM) was proposed to simultaneously maintain the second order accuracy for both the interface and its curvature [29]. Barret *et al.* [30] developed a variational formulation for interface evolution which allows for tangential movement of interfacial markers. This method has the advantage of nearly equidistribution of interfacial markers and thus avoids the artificial marker redistribution. Besides its successful applications in the geometric evolution equations, PFEM has also been extended to fit the MCL problems in the contexts of solid state dewetting [31] and two-phase flows [32].

In this paper, we take the advantage of both IIM and PFEM to develop a second order accurate method to solve the Stokes problems with Navier-slip boundary condition and contact angle condition. For the Stokes equation with Navier-slip boundary condition, we generalize IIM to solve for the velocity field to the second order accuracy on a staggered grid. Correction terms for irregular points are introduced through jump conditions using Taylor expansions at interfacial points. Necessary adjustments are made nearby the contact lines to account for the Navier-slip boundary condition. In order to accurately compute the curvature at the markers, we reformulate the interfacial kinematic condition and the contact angle condition in a variational form. The unbalanced Young's stress enters the evolution equation of the interface after an integration by parts. We apply PFEM to solve for the interface motion and the curvature at the same time. After appropriate interpolation of the velocity field and temporal discretization, we combine the resulting finite difference scheme for velocity field and finite element framework for interfacial evolution, and obtain a unified scheme. This scheme is expected to inherit the advantage of the second order accuracy from both IIM and PFEM, and predict the contact line motion accurately in second order. This is validated by our numerical simulations. We present the numerical result of the droplet motion on a chemically heterogeneous surface. Due to the second order accuracy of the proposed scheme, we could study the contact line dynamics on the substrate which has periodic chemical patterns with very small period. Stick-slip phenomenon and contact angle hysteresis are observed. We also numerically investigate sliding dynamics and Kelvin pendant, and generalize the method to the case of discontinuous viscosity.

This paper is organized as follows. The mathematical formulation is introduced in Section 2. We then present the IIM for the two-phase Stokes problem and the PFEM for the moving interface in Section 3. The two methods are coupled after a proper treatment of the interaction terms. In

Section 4, we present numerical examples and validated the second order accuracy of both velocity field and the interface positions numerically. Conclusions and discussions are made in Section 5. Technical derivations of the jump terms are given in appendices.

2. Mathematical formulation

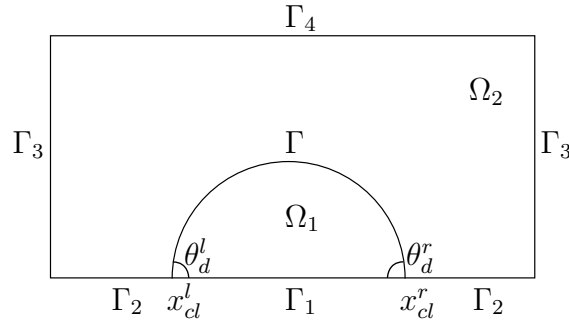### 2.1. 2D Stokes flow with Navier-slip boundary condition

Figure 1: The Stokes flow.

We consider the two-dimensional two-phase Stokes flow as depicted in Figure 1:

$$-\nabla p + \nabla \cdot \mathbf{T}_i = 0, \tag{2}$$
$$\nabla \cdot \mathbf{u} = 0, \tag{3}$$

in the fluids $\Omega_i (i = 1, 2)$, where p is the pressure, $\mathbf{u} = (u, v)^\top$ is the velocity field, and $\mathbf{T}_i$ are the Newtonian viscous stress tensor

$$\mathbf{T}_i = \nu_i \left(\nabla \mathbf{u} + (\nabla \mathbf{u})^\top \right), \tag{4}$$

with $\nu_i (i = 1, 2)$ being the viscosity of fluid in Ω_i. In this paper, we assume the viscosity ν_i are both constants.

Across the interface Γ, the jump condition is given by

$$\mathbf{n} \cdot [-p\mathbf{I} + \mathbf{T}_i] \cdot \mathbf{n} = -\gamma \kappa, \quad \mathbf{n} \cdot [\mathbf{T}_i] \cdot \boldsymbol{\tau} = 0, \tag{5}$$

where γ is the surface tension coefficient, κ is the curvature of interface, $\mathbf{n}$ and $\boldsymbol{\tau}$ are the normal and tangent unit vectors, and $[\cdot]$ denotes the jump across the interface from Ω_1 to Ω_2, i.e., $[\mathbf{T}_i] = \mathbf{T}_2 - \mathbf{T}_1$.

5

No-penetration conditions are imposed on top and bottom boundaries

$$\mathbf{u} \cdot \mathbf{n} = 0. \tag{6}$$

Slip model is introduced by the Navier-slip boundary condition (NBC):

$$\boldsymbol{\tau} \cdot \mathbf{T}_i \cdot \mathbf{n} = -\beta_i \mathbf{u}_s, \tag{7}$$

where $\mathbf{u}_s$ is the slip velocity of fluid and $\beta_i(i = 1, 2)$ are friction coefficients between each fluid and solid substrate.

The contact angle condition (CAC) is imposed at the contact line:

$$\gamma \left(\cos \theta_d - \cos \theta_y \right) = -\beta_{cl} u_{cl}, \tag{8}$$

where u_{cl} is the contact line velocity, β_{cl} is the friction coefficient between the interface and the substrate, θ_d is the dynamic contact angle, and θ_y has been defined in (1).

For simplicity, we assume the periodic conditions hold on the left and right boundaries, while the no-slip condition holds on the top boundary.

Furthermore, the interface evolution is described by the kinematic condition

$$\frac{\partial \mathbf{X}}{\partial t} \cdot \mathbf{n} = \mathbf{u} \left(\mathbf{X}, t \right) \cdot \mathbf{n}, \tag{9}$$

where $\mathbf{X}(s, t)$ is the position vector of the interface and is parameterized by the arclength s.

2.2. The dimensionless model

In this paper, we solve the governing equations and the interface/boundary conditions in their dimensionless form. To obtain the dimensionless equations, we define the dimensionless variables as

$$\nu_i^* = \frac{\nu_i}{\nu_1}, \ \beta_i^* = \frac{\beta_i}{\beta_1}, \ \gamma_i^* = \frac{\gamma_i}{\gamma}, \ \beta_{cl}^* = \frac{\beta_{cl}}{\nu_1}, \ \kappa^* = L\kappa, \ \mathbf{x}^* = \frac{\mathbf{x}}{L}, \ \mathbf{u}^* = \frac{\mathbf{u}}{U},$$

$$t^* = \frac{t}{L/U}, \ p^* = \frac{p}{\nu_1 U/L}, \ \lambda_i = \frac{\nu_i/\nu_1}{\beta_i/\beta_1}, \ Ca = \frac{\nu_1 U}{\gamma}, \ l_s = \frac{\nu_1}{\beta_1 L},$$

where L and U are the characteristic length and characteristic speed of the system, Ca and l_s are the Capillary number and slip length. Assume the

friction coefficients are equal, i.e., $\beta_1 = \beta_2$, so that $\lambda_1 = 1, \lambda_2 = \nu_2^*$. Then the Stokes equations (2)-(3) are recast in the dimensionless form

$$-\nu_i \Delta \mathbf{u} + \nabla p = 0, \tag{10}$$
$$\nabla \cdot \mathbf{u} = 0, \tag{11}$$

where the divergence free condition has been used to obtain the first equation. The asterisk symbols $(*)$ are omitted for simplicity. The interface condition at Γ becomes

$$\mathbf{n} \cdot [-p\mathbf{I} + \mathbf{T}_i] \cdot \mathbf{n} = -\frac{1}{Ca}\kappa, \quad \mathbf{n} \cdot [\mathbf{T}_i] \cdot \boldsymbol{\tau} = 0. \tag{12}$$

The dimensionless NBC (7) and other conditions are imposed on the boundaries

(BC1): $u = \lambda_i l_s \dfrac{\partial u}{\partial y}, v = 0, \text{ on } \Gamma_1 \cup \Gamma_2(\text{bottom boundary}),$ \hfill (13)

(BC2): $\mathbf{u}$ and p are periodic on Γ_3(left and right boundaries), \hfill (14)

(BC3): $\mathbf{u} = 0, \text{ on } \Gamma_4(\text{top boundary}).$ \hfill (15)

Non-dimensional form of the CAC (8) is

$$\beta_{cl}^* Ca \frac{\mathrm{d}x_{cl}^l}{\mathrm{d}t} = \cos\theta_d^l - \cos\theta_y, \quad -\beta_{cl}^* Ca \frac{\mathrm{d}x_{cl}^r}{\mathrm{d}t} = \cos\theta_d^r - \cos\theta_y, \tag{16}$$

where x_{cl}^l and x_{cl}^r are left and right contact points, and θ_d^l and θ_d^r are left and right dynamic contact angles.

3. Numerical methods

In this section, we demonstrate the numerical scheme to simulate the droplet motion on a solid substrate. By introducing the correction terms, we present the IIM scheme in Section 3.1. As the correction terms depend on the interface geometries, the second order accuracy of the position and curvature of the interface is necessary to solve the velocity field to second order accuracy. This can be achieved by the PFEM scheme which we introduce in Section 3.2. The coupling of the two schemes requires an appropriate interpolation of the velocity field. The interpolation scheme along with other technical issues in the coupling can be found in Section 3.3.

3.1. Correction terms and IIM scheme

A classical Marker-and-Cell (MAC) staggered grid is used to solve the Stokes equations (10)-(11). The computational domain $[-1,1] \times [0,1]$ is covered by a uniform staggered grid, i.e., $\Delta x = \Delta y = h$. We define the grid points $(x_i, y_j) = (-1 + ih, jh)$ for $i = 0, 1, 2, \cdots, N_x$ and $j = 0, 1, 2, \cdots, N_y$, and the midpoints at x- direction and y- direction as $x_{i+\frac{1}{2}} = -1 + (i + \frac{1}{2})h$ and $y_{j+\frac{1}{2}} = (j + \frac{1}{2})h$. $u_{i,j}$, $v_{i,j}$, and $p_{i,j}$ are the approximations of the point values $u(x_i, y_{j+\frac{1}{2}})$, $v(x_{i+\frac{1}{2}}, y_j)$, and $p(x_{i+\frac{1}{2}}, y_{j+\frac{1}{2}})$ respectively as shown in the left panel of Figure 2. An advantage of using staggered grid is that no artificial boundary condition is needed for the pressure field.
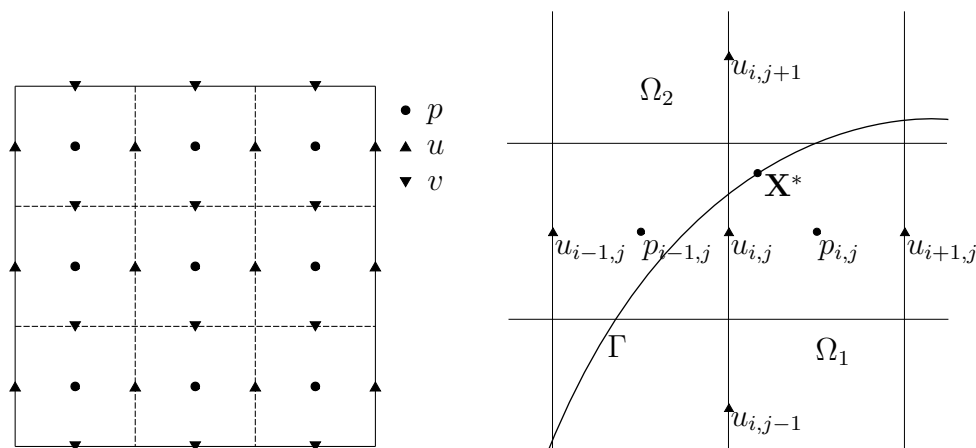

Figure 2: The left panel shows the location of p, u, v. The right panel gives an example in which $u_{i,j}$ locates at an irregular point.

Once the grid is set, the grid points are classified into regular and irregular points. When the five points of the standard discrete Laplacian scheme do not stay on the same side of interface, the central grid point is called an irregular point (e.g., $u_{i,j}$ locates at an irregular point in the right panel of Figure 2). Otherwise, it is regular.

The jump conditions across the interface Γ for the Stokes equations (10)-(11) are summarized as follows

$$[p] = 2\left[\nu_i \frac{\partial \mathbf{u}}{\partial n} \cdot \mathbf{n}\right] + \frac{\kappa}{Ca}, \tag{17}$$

$$\left[\frac{\partial p}{\partial n}\right] = 2\left[\nu_i \frac{\partial^2 \mathbf{u}}{\partial s^2} \cdot \mathbf{n}\right] - 4\kappa\left[\nu_i \frac{\partial \mathbf{u}}{\partial s} \cdot \boldsymbol{\tau}\right], \tag{18}$$

8

$$\left[\nu_i \frac{\partial \mathbf{u}}{\partial n} \cdot \boldsymbol{\tau} \right] + \left[\nu_i \frac{\partial \mathbf{u}}{\partial s} \cdot \mathbf{n} \right] = 0. \tag{19}$$

(17) and (19) are the consequences of force balance on the interface in the normal and tangential directions. (18) is derived from the Stokes equation (10) in local coordinates under appropriate regularity conditions on $\mathbf{u}$. The derivations can be found in the Appendix A. We also refer a derivation through tensor analysis in [33].

In the case of continuous viscosity, $\left[\nu_i \frac{\partial \mathbf{u}}{\partial s} \right] = 0$. By using the incompressibility condition (11), we have

$$\left[\nu_i \frac{\partial \mathbf{u}}{\partial n} \cdot \mathbf{n} \right] = 0, \quad 2 \left[\nu_i \frac{\partial^2 \mathbf{u}}{\partial s^2} \cdot \mathbf{n} \right] - 4\kappa \left[\nu_i \frac{\partial \mathbf{u}}{\partial s} \cdot \boldsymbol{\tau} \right] = 0. \tag{20}$$

Then we recover the jump conditions for continuous viscosity as in [34]:

$$[p](s) = \frac{\kappa}{Ca}, \qquad \left[\frac{\partial p}{\partial n} \right](s) = 0, \qquad \left[\frac{\partial u}{\partial n} \right](s) = 0, \qquad \left[\frac{\partial v}{\partial n} \right](s) = 0. \tag{21}$$

Based on these conditions, correction terms at irregular points can be derived using Taylor expansions at the orthogonal projection onto the interface [27]. However, in MCL problems, there may be no projection on the interface for irregular points near contact lines. For instance, when the contact angle is less than 90°, the projection of some irregular point nearby the contact lines is out of domain.

To avoid this issue, it is more convenient to introduce a different "projection point" $\mathbf{X}^*$ on the interface, and define the correction terms through the jump conditions at $\mathbf{X}^*$ in x- and y- partial derivatives. For instance, the correction term for u at $(x_i, y_{j+\frac{1}{2}})$ is represented as

$$\begin{aligned}
u_{i,j}^c =& [u]_{\mathbf{X}^*} + (x_i - x^*) \left[\frac{\partial u}{\partial x} \right]_{\mathbf{X}^*} + (y_{j+\frac{1}{2}} - y^*) \left[\frac{\partial u}{\partial y} \right]_{\mathbf{X}^*} + \frac{1}{2} \left((x_i - x^*)^2 \left[\frac{\partial^2 u}{\partial x^2} \right]_{\mathbf{X}^*} \right. \\
&\left. + 2(x_i - x^*)(y_{j+\frac{1}{2}} - y^*) \left[\frac{\partial^2 u}{\partial x \partial y} \right]_{\mathbf{X}^*} + (y_{j+\frac{1}{2}} - y^*)^2 \left[\frac{\partial^2 u}{\partial y^2} \right]_{\mathbf{X}^*} \right) + \mathcal{O}\left(h^3\right).
\end{aligned} \tag{22}$$

Here $\mathbf{X}^*$ is a point on the interface close to $(x_i, y_{j+\frac{1}{2}})$ and we will illustrate how to choose $\mathbf{X}^*$ in Section 3.3. The correction terms for v and p can be defined in a similar manner. However, since the derivative of the pressure

9

is one order lower than that of the velocity field in the Stokes equation, the correction terms for p only need to be expanded to the first order, i.e.,

$$p_{i,j}^c = [p]_{\mathbf{X}^*} + (x_{i+\frac{1}{2}} - x^*) \left[\frac{\partial p}{\partial x}\right]_{\mathbf{X}^*} + (y_{j+\frac{1}{2}} - y^*) \left[\frac{\partial p}{\partial y}\right]_{\mathbf{X}^*} + \mathcal{O}\left(h^2\right). \quad (23)$$

Using the coordinate transformation, the jumps in the velocity field, the pressure field, and their x- and y- partial derivatives can be represented using normal and tangential derivatives. The detail derivations can be found in Appendix B.

We are ready to give the discretization scheme. Let $(x_i, y_{j+\frac{1}{2}})$ be an irregular point in Ω_1 as shown in the right panel of Figure 2. Define the modified values after corrections as

$$\tilde{u}_{i-1,j} = u_{i-1,j} - u_{i-1,j}^c, \quad \tilde{u}_{i,j+1} = u_{i,j+1} - u_{i,j+1}^c, \quad (24)$$

which mimic the values as if there are no jumps in the variable u and its derivatives. Then the Laplacian $\Delta u(x_i, y_{j+\frac{1}{2}})$ can be approximated as

$$\Delta u(x_i, y_{j+\frac{1}{2}}) = \frac{\tilde{u}_{i-1,j} - 2u_{i,j} + u_{i+1,j}}{h^2} + \frac{\tilde{u}_{i,j+1} - 2u_{i,j} + u_{i,j-1}}{h^2} + \mathcal{O}\left(h^2\right)$$

$$= \Delta_h u_{i,j} - \frac{u_{i-1,j}^c}{h^2} - \frac{u_{i,j+1}^c}{h^2} + \mathcal{O}\left(h^2\right),$$

where $\Delta_h u_{i,j}$ is the standard five point stencil for Laplacian operator. Similarly, we have finite difference approximations for other quantities, for instance,

$$\frac{\partial p}{\partial x}(x_i, y_j) = \frac{p_{i,j} - p_{i-1,j}}{h} + \frac{p_{i-1,j}^c}{h} + \mathcal{O}\left(h^2\right).$$

As a result, the finite difference scheme for the incompressible Stokes equations can be written as

$$-\Delta_h u_{i,j} + \frac{p_{i,j} - p_{i-1,j}}{h} = C\{\Delta_h u\}_{i,j} - C\left\{\frac{\partial p}{\partial x}\right\}_{i,j}, \quad (25)$$

$$-\Delta_h v_{i,j} + \frac{p_{i,j} - p_{i,j-1}}{h} = C\{\Delta_h v\}_{i,j} - C\left\{\frac{\partial p}{\partial y}\right\}_{i,j}, \quad (26)$$

$$\frac{u_{i+1,j} - u_{i,j}}{h} + \frac{v_{i,j+1} - v_{i,j}}{h} = -C\{\nabla_h \cdot \mathbf{u}\}_{i,j}, \quad (27)$$

10

where $C\{\cdot\}$ denote the correction terms which are not zero only at the irregular points. From (22), we can see these correction terms depend on the interfacial geometries, such as the position and the curvature, through the jump terms. A compatibility condition should be satisfied in (27), specifically,

$$\sum_{i,j} C\{\nabla_h \cdot \mathbf{u}\}_{i,j} = 0.$$

In order to achieve second order accuracy in approximating the velocity field, IIM scheme requires $\mathcal{O}\left(h\right)$ truncation error at the irregular points and $\mathcal{O}\left(h^2\right)$ truncation error at the regular points. This can be achieved if we can approximate $u_{i,j}^c$ within $\mathcal{O}\left(h^3\right)$ accuracy and $p_{i,j}^c$ within $\mathcal{O}\left(h^2\right)$ accuracy respectively. By (22) and (23), we need to approximate the jump terms $\left[\frac{\partial u}{\partial x}\right]_{\mathbf{X}^*}$, $\left[\frac{\partial u}{\partial y}\right]_{\mathbf{X}^*}$, $[p]_{\mathbf{X}^*}$ within second order accuracy, and $\left[\frac{\partial^2 u}{\partial x^2}\right]_{\mathbf{X}^*}$, $\left[\frac{\partial^2 u}{\partial x \partial y}\right]_{\mathbf{X}^*}$, $\left[\frac{\partial^2 u}{\partial y^2}\right]_{\mathbf{X}^*}$, $\left[\frac{\partial p}{\partial x}\right]_{\mathbf{X}^*}$, $\left[\frac{\partial p}{\partial y}\right]_{\mathbf{X}^*}$ within first order accuracy respectively. A detailed check of the jump conditions in Appendix B shows that these can be satisfied if the interface position vector $\mathbf{X}$ and the curvature κ can be solved in second order accuracy. We will discuss how to solve $\mathbf{X}$ and κ using PFEM in the next subsection.

To discretize the NBC (13), a ghost value $u_{i,-1}$ is introduced at $(x_i, y_{-\frac{1}{2}})$. Then the finite difference scheme of the NBC away from the contact line is

$$\frac{u_{i,-1} + u_{i,0}}{2} = \lambda_i l_s \frac{u_{i,0} - u_{i,-1}}{h}. \tag{28}$$

Thanks to the introduction of the ghost value $u_{i,-1}$, correction terms can be similarly defined at the irregular points nearby the contact line.

3.2. Evolution of the interface and moving contact line

We introduce the equations which describe the evolution of the interface $\mathbf{X}(s,t)$,

$$\frac{\partial \mathbf{X}}{\partial t} \cdot \mathbf{n} = \mathbf{U} \cdot \mathbf{n}, \tag{29}$$

$$\kappa \mathbf{n} = \frac{\partial^2 \mathbf{X}}{\partial s^2}, \tag{30}$$

where s is the arclength parameter, and $\mathbf{U} = \mathbf{u}|_\Gamma$ is the velocity on the interface. The second equation is the definition of the curvature. We aim to obtain second order accurate approximations of the interface and its curvature.

11

In order to apply PFEM, we need to reformulate (29), (30) and the CAC (16) in the weak sense. We first introduce $\rho \in I := [0,1]$ to parameterize the interface clockwise. Then the arclength is $s(\rho, t) = \int_0^\rho |\frac{\partial \mathbf{X}}{\partial \rho}| \mathrm{d}\rho$ and $\frac{\partial s}{\partial \rho} = |\frac{\partial \mathbf{X}}{\partial \rho}|$, where the subscript ρ denotes the derivative with respect to ρ. The L^2 inner product on the interface is defined as

$$(f, g)_\Gamma = \int_{\Gamma(t)} f(s) \cdot g(s) \mathrm{d}s = \int_I f(s(\rho, t)) \cdot g(s(\rho, t)) \left| \frac{\partial \mathbf{X}}{\partial \rho} \right| \mathrm{d}\rho.$$

Define the function space

$$H_0^1(I) = \{\phi \in H^1(I) : \phi(0) = \phi(1) = 0\},$$

where $H^1(I)$ is the standard Sobolev space. After integration by parts, we obtain the interface evolution equation in the weak form

$$\left(\frac{\partial \mathbf{X}}{\partial t} \cdot \mathbf{n}, \phi \right)_\Gamma - (\mathbf{U} \cdot \mathbf{n}, \phi)_\Gamma = 0, \ \forall \phi \in H^1(I), \tag{31}$$

$$(\kappa \mathbf{n}, \mathbf{g})_\Gamma + \left(\frac{\partial \mathbf{X}}{\partial s}, \frac{\partial \mathbf{g}}{\partial s} \right)_\Gamma - \left(\frac{\partial x}{\partial s} \cdot g_1 \right) \Big|_{\rho=0}^{\rho=1} = 0, \ \forall \mathbf{g} \in H^1(I) \times H_0^1(I), \tag{32}$$

where $\frac{\partial \mathbf{X}}{\partial s} = \frac{\partial \mathbf{X}/\partial \rho}{|\partial \mathbf{X}/\partial \rho|}$. Using the geometrical relation that $\cos \theta_d^l = \frac{\partial x}{\partial s}\big|_{\rho=0}$, $\cos \theta_d^r = \frac{\partial x}{\partial s}\big|_{\rho=1}$ and the CAC (16), we reorganize (32) as

$$(\kappa \mathbf{n}, \mathbf{g})_\Gamma + \left(\frac{\partial \mathbf{X}}{\partial s}, \frac{\partial \mathbf{g}}{\partial s} \right)_\Gamma - (\cos \theta_y \cdot g_1) \Big|_{\rho=0}^{\rho=1} + \beta_{cl}^* Ca \left(\frac{\mathrm{d}x_{cl}^l}{\mathrm{d}t} g_1(0) + \frac{\mathrm{d}x_{cl}^r}{\mathrm{d}t} g_1(1) \right) = 0.$$

Now we are ready to apply PFEM. First introduce the decomposition $I = \cup_{k=1}^K I_k$ as a disjoint union, and define the finite element spaces as

$$V^h := \{\phi \in C(I) : \phi|_{I_k} \in P_1, k = 1, 2, \cdots, K\} \subset H^1(I),$$
$$V_0^h := \{\phi \in V^h : \phi(0) = \phi(1) = 0\} \subset H_0^1(I),$$

where P_1 denotes all polynomials with degrees at most one. Let $\mathbf{X}^m$, $\mathbf{n}^m$, $\mathbf{U}^m$, and κ^m be the numerical approximations of the interface $\mathbf{X}(\cdot, t_m)$, the unit normal vector $\mathbf{n}$, the velocity $\mathbf{U}$ on the interface, and the curvature κ at time $t_m = m\tau$ respectively, where the time step size is uniform $\Delta t = \tau$. Then the approximation scheme of the interface evolution (29)-(30) is given by:

12

Given $\mathbf{X}^m$, $\mathbf{n}^m$, and $\mathbf{U}^m$ at time t_m, find $\mathbf{X}^{m+1} \in V^h \times V_0^h$, $\kappa^{m+1} \in V^h$,

$$\left(\frac{\mathbf{X}^{m+1} - \mathbf{X}^m}{\tau}\mathbf{n}^m, \phi\right)_{\Gamma^m} - (\mathbf{U}^m \cdot \mathbf{n}^m, \phi)_{\Gamma^m} = 0, \ \forall \phi \in V^h, \tag{33}$$

$$\left(\kappa^{m+1}\mathbf{n}^m, \mathbf{g}\right)_{\Gamma^m} + \left(\frac{\partial \mathbf{X}^{m+1}}{\partial s}, \frac{\partial \mathbf{g}}{\partial s}\right)_{\Gamma^m} - (\cos\theta_y \cdot g_1)\Big|_{\rho=0}^{\rho=1}$$
$$+ \beta_{cl}^* Ca \left(\frac{x_l^{m+1} - x_l^m}{\tau}g_1(0) + \frac{x_r^{m+1} - x_r^m}{\tau}g_1(1)\right) = 0, \ \forall \mathbf{g} \in V^h \times V_0^h. \tag{34}$$

Here $\mathbf{U}^m = \mathbf{G}(\mathbf{u}^m)$ is interpolated from the velocity field on the grid with $\mathbf{G}$ being the interpolation operator. The interpolation technique will be discussed in detail in the next subsection.

For simplicity, the forward Euler method has been used to do temporal discretization here. We will discuss other temporal discretization in the next subsection. It is worth noting that the contact angle condition is naturally imposed in this way and integrated with the interface motion.

3.3. Complete Algorithm

We now combine IIM and PFEM to give the complete algorithm from time step t_m to t_{m+1}. At $t_m = m\tau$, given the interface profile $\mathbf{X}^m$ and its curvature κ^m, we carry out following steps:

Step 1: Update velocity by solving the Stokes flow using IIM

$$-\Delta_h u_{i,j}^m + \frac{p_{i,j}^m - p_{i-1,j}^m}{h} = C\{\Delta_h u^m\}_{i,j} - C\left\{\frac{\partial p^m}{\partial x}\right\}_{i,j}, \tag{35}$$

$$-\Delta_h v_{i,j}^m + \frac{p_{i,j}^m - p_{i,j-1}^m}{h} = C\{\Delta_h v^m\}_{i,j} - C\left\{\frac{\partial p^m}{\partial y}\right\}_{i,j}, \tag{36}$$

$$\frac{u_{i+1,j}^m - u_{i,j}^m}{h} + \frac{v_{i+1,j}^m - v_{i,j}^m}{h} = -C\{\nabla_h \cdot \mathbf{u}^m\}_{i,j}, \tag{37}$$

where the correction terms $C\{\cdot\}$ depend on $\mathbf{X}^m$ and κ^m, and are calculated as illustrated in Section 3.1;

Step 2: Update interface using PFEM

$$\left(\frac{\mathbf{X}^{m+1} - \mathbf{X}^m}{\tau}\mathbf{n}^m, \phi\right)_{\Gamma^m} - (\mathbf{U}^m \cdot \mathbf{n}^m, \phi)_{\Gamma^m} = 0, \ \forall \phi \in V^h, \tag{38}$$

13

$$\left(\kappa^{m+1}\mathbf{n}^m, \mathbf{g}\right)_{\Gamma^m} + \left(\frac{\partial \mathbf{X}^{m+1}}{\partial s}, \frac{\partial \mathbf{g}}{\partial s}\right)_{\Gamma^m} - \left.(\cos\theta_y \cdot g_1)\right|_{\rho=0}^{\rho=1}$$

$$+ \beta_{cl}^* Ca \left(\frac{x_l^{m+1} - x_l^m}{\tau} g_1(0) + \frac{x_r^{m+1} - x_r^m}{\tau} g_1(1)\right) = 0, \ \forall \mathbf{g} \in V^h \times V_0^h, \tag{39}$$

where $\mathbf{U}^m = \mathbf{G}(\mathbf{u}^m)$ is interpolated from the velocity field on the grid.

We are still left with some issues in this scheme. The first one is the selection of the "projection point" $\mathbf{X}^*$, and the computation of the normal vector $\mathbf{n}^m$ and the derivative $\frac{\partial \kappa^m}{\partial s}$ in the correction terms. In our method, the normal unit vectors $\mathbf{n}^m$ are defined on piecewise line segments naturally, i.e., each line segment corresponds to a unique normal vector. To approximate the correction terms, a straightforward way is to choose the closest midpoint of the line segments as $\mathbf{X}^*$ in (22). Since the curvature κ^m obtained from (38)-(39) is piecewise linear on Γ^m, its derivative $\frac{\partial \kappa^m}{\partial s}$ at $\mathbf{X}^*$ is computed directly.

The second issue is the interpolation of the interface velocity $\mathbf{U}^m = \mathbf{G}(\mathbf{u}^m)$ from the velocity field $\mathbf{u}^m$ on the Cartesian grid. As the velocity field is not smooth across the interface, standard interpolation techniques are not sufficient to guarantee second order accuracy, and jump conditions need to be taken into account. We use a modified bilinear interpolation [27], whose idea essentially lies in a second order correction in the velocity field across the interface. For instance, if we treat the velocity values at the grid points in the inside region Ω_1 as the reference values, then any velocity values at the grid points in Ω_2 nearby the interface should be modified by adding a correction term:

$$u_{i,j}^c = [u]_{\mathbf{X}^*} + (x_i - x^*)\left[\frac{\partial u}{\partial x}\right]_{\mathbf{X}^*} + (y_{j+\frac{1}{2}} - y^*)\left[\frac{\partial u}{\partial y}\right]_{\mathbf{X}^*} + \mathcal{O}\left(h^2\right).$$

After the corrections, bilinear interpolation can be applied to obtain the interfacial values by using the corrected values and the reference values. It should be noted that in the case of continuous viscosity across the interface, (B.2) implies no jumps in $[u]_{\mathbf{X}^*}$, $\left[\frac{\partial u}{\partial x}\right]_{\mathbf{X}^*}$, and $\left[\frac{\partial u}{\partial y}\right]_{\mathbf{X}^*}$. Thus any second order interpolation would work. So far, the whole algorithm is complete as shown in Algorithm 1.

To enhance the computational efficiency and accuracy in time, we can use the second order Runge-Kutta (RK2) scheme for the temporal discretization. Starting from t_m, we first solve for velocity field $\mathbf{u}^m$ and use it to obtain a half-step interface $\mathbf{X}^{m+\frac{1}{2}}$ along with its curvature $\kappa^{m+\frac{1}{2}}$. An intermediate

14

velocity field $\mathbf{u}^{m+\frac{1}{2}}$ is thus solved. This velocity field is then interpolated to obtain the interface velocity which is used to update the interface from t_m:

$$\left(\frac{\mathbf{X}^{m+1} - \mathbf{X}^m}{\tau}\mathbf{n}^m, \phi\right)_{\Gamma^m} - \left(\mathbf{U}^{m+\frac{1}{2}} \cdot \mathbf{n}^m, \phi\right)_{\Gamma^m} = 0.$$

Algorithm 1 Complete Algorithm from time step t_m to t_{m+1}

1: Given $\mathbf{X}_m$ and κ^m, compute $\mathbf{n}^m$ and $\frac{\partial \kappa^m}{\partial s}$ at midpoint of the line segments
2: Compute the correction terms $C\{\cdot\}$ and calculate the velocity $\mathbf{u}^m$ using IIM
3: Interpolate the velocity filed $\mathbf{u}^m$ to the velocity $\mathbf{U}^m$ at interface
4: Update the interface $\mathbf{X}^{m+1}$ and the curvature κ^{m+1} using PFEM

So far we have concentrated on the case of continuous viscosity. If the viscosity is discontinuous across the interface, (20) no longer holds and the derivation of correction terms become more involved. However, we can simplify the formulation by introducing an augmented variable $\mathbf{q} = [\nu_i \mathbf{u}]$ [35]. Then the jump conditions become

$$[p] = 2\frac{\partial \mathbf{q}}{\partial n} \cdot \mathbf{n} + \frac{\kappa}{Ca}, \quad \left[\frac{\partial p}{\partial n}\right] = 2\frac{\partial^2 \mathbf{q}}{\partial s^2} \cdot \mathbf{n} - 4\kappa\frac{\partial \mathbf{q}}{\partial s} \cdot \boldsymbol{\tau}, \tag{40}$$

$$[\hat{u}] = q_1, \quad \left[\frac{\partial \hat{u}}{\partial n}\right] = \left(\frac{\partial \mathbf{q}}{\partial s} \cdot \mathbf{n}\right)\sin\psi - \left(\frac{\partial \mathbf{q}}{\partial s} \cdot \boldsymbol{\tau}\right)\cos\psi, \tag{41}$$

$$[\hat{v}] = q_2, \quad \left[\frac{\partial \hat{v}}{\partial n}\right] = -\left(\frac{\partial \mathbf{q}}{\partial s} \cdot \mathbf{n}\right)\cos\psi - \left(\frac{\partial \mathbf{q}}{\partial s} \cdot \boldsymbol{\tau}\right)\sin\psi, \tag{42}$$

where we have defined the modified velocity field $\hat{\mathbf{u}} = \nu_i \mathbf{u}$. With the help of the modified velocity field, all the correction terms can be derived in a similar way as before. As a result, we obtain a finite difference scheme of the Stokes equation using correction terms to solve for the modified velocity field $\hat{\mathbf{u}}$, the pressure field p, and augmented variables $\mathbf{q}$. This system of equations is closed after imposing the constraint

$$[\mathbf{u}] = [\hat{\mathbf{u}}/\nu_i] = 0,$$

which comes from the continuity of the original velocity field. The system is linear and can be solved using GMRES.

4. Numerical results

In this section, we present numerical studies on MCL problems. Numerical simulations are performed on a staggered grid in $[-1, 1] \times [0, 1]$. The Capillary number and slip length are $Ca = 0.1$ and $l_s = 0.1$ respectively in the following experiments unless otherwise specified. Viscosities are constants except in the last example. In this section, we first present the benchmark problem of droplet relaxation as the convergence test. Then the algorithm is applied to investigate sliding droplets, Kelvin pendant and CAH on chemically heterogeneous surface. We also simulate the two-phase MCL problems with discontinuous viscosity.

Example 1 (Droplet spreading) As a first example, we perform a standard convergence test in which the droplet relaxation process on a substrate is simulated with $\theta_y = 90°$. The initial state of the interface is part of a circle with contact angle $\theta_{in} = 60°$. The droplet then relaxes to a semi-circular shape driven by the contact line dynamics. The computation is performed on different grids $N_x \times N_y = 32 \times 16, 64 \times 32, 128 \times 64, 256 \times 128$ and 512×256. We choose the solution computed on the grid $N_x \times N_y = 512 \times 256$ as the reference solution. Table 1 summarizes the errors and their corresponding orders at $t = 1.2$. The convergence orders of the interface and the velocity field are second order. The numerical error of the interface at time level t_m in l_∞ norm can be measured as [29, 30, 31]

$$\|E_{\mathbf{X}}(t_m)\|_\infty = \max_{0 \le k \le K} \min_{\rho \in [0,1]} \left| \mathbf{X}^m(\rho_k) - \mathbf{X}_{ref}^m(\rho) \right|,$$

where the curve $\mathbf{X}_{ref}^m(\rho)$ is computed on $N_x \times N_y = 512 \times 256$.

Our method also preserves the equidistribution property of PFEM. Define the mesh distribution function at time level t_m as [31]

$$\Psi^m := \frac{\max_{1 \le k \le K} \left| \mathbf{X}^m(\rho_k) - \mathbf{X}^m(\rho_{k-1}) \right|}{\min_{1 \le k \le K} \left| \mathbf{X}^m(\rho_k) - \mathbf{X}^m(\rho_{k-1}) \right|}.$$

From Figure 3, we can see the function increases firstly, then gradually decreases in a long time and finally converges to 1, i.e., $\Psi^m \to 1$ when $m \to \infty$. The interface markers initially are not equally distributed due to the contact line dynamics. The non-equidistribution is gradually remedied by the PFEM.

Example 2 (Droplet on a slope) We present a droplet, which is driven by gravity, sliding on a sloping substrate in this example. To simulate a droplet

16

$N_x \times N_y$	$\|E_u\|_2$	order$_u$	$\|E_v\|_2$	order$_v$
32×16	1.2252×10^{-4}		1.1416×10^{-4}	
64×32	3.7179×10^{-5}	1.7204	3.5075×10^{-5}	1.7025
128×64	9.2832×10^{-6}	2.0018	8.7595×10^{-6}	2.0015
256×128	2.0272×10^{-6}	2.1951	1.9253×10^{-6}	2.1858
$N_x \times N_y$	$\|E_{\mathbf{X}}\|_\infty$	order$_{\mathbf{X}}$	$\|E_{cl}\|_\infty$	order$_{cl}$
32×16	3.1641×10^{-3}		3.1641×10^{-3}	
64×32	8.9232×10^{-4}	1.8262	8.8346×10^{-4}	1.8405
128×64	2.2667×10^{-4}	1.9770	2.1429×10^{-4}	2.0436
256×128	5.3114×10^{-5}	2.0934	4.4977×10^{-5}	2.2523

Table 1: Errors and convergence order of velocity fields, interface and contact lines. Absolute errors are computed by comparing with the reference solution computed on $N_x \times N_y = 512 \times 256$. E_u, E_v, $E_{\mathbf{X}}$, and E_{cl} denote the absolute errors of velocity field u, v, the interface $\mathbf{X}$, and the left contact line position x_{cl} respectively. $\|\cdot\|_2$ and $\|\cdot\|_\infty$ denote l_2 and l_∞ norms.

on a sloping substrate, a gravity force is added as the body force in the Stokes equations. Taking into account the rotation of the coordinate system, (10) is modified to

$$-\nu_i \Delta \mathbf{u} + \nabla p = \frac{Bo}{Ca} \left(\sin \theta_{slope}, -\cos \theta_{slope} \right)^\top,$$

where θ_{slope} is the tilt angle of substrate, and $Bo = \frac{\Delta \rho g L^2}{\gamma_3}$ is the Bond number with $\Delta \rho$ being the difference in density of the two fluids and g being the gravitational acceleration.

We place a droplet with a semi-circular interface on the slope. The Young's angle is set to $\theta_y = 90°$. Without gravity, the droplet should be in a steady state. When the gravity is introduced, we see in Figure 4 that the droplet slides downward due to the gravity and the two contact angles change simultaneously. The advancing angle in the moving front is increasing while the receding angle in the tail is decreasing. Both angles reach their steady values after a while, and the droplet moves downwards at a constant speed (inside figure) while the shape of the interface remains almost unchanged.

Example 3 (Kelvin pendant droplets) Lord Kelvin geometrically constructs droplet profiles with "repeated bulges" that are known by his name [36]. This can be treated as a special case of the previous example. In this
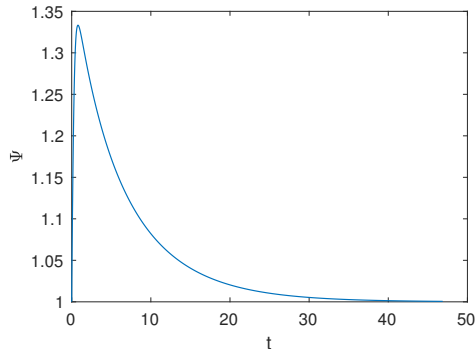
Figure 3: The temporal evolution of the mesh distribution function $\Psi(t)$.

example, the droplets are suspended from the ceiling, i.e., $\theta_{slope} = 180°$. The initial droplet profile is part of a circle with contact angle $\theta_{in} = 30°$ as shown by the blue curve in Figure 5. We consider both hydrophilic and hydrophobic cases. In the hydrophilic case with Bond number $Bo = 20$ and Young's angle $\theta_y = 60.75°$, the droplet is stretched due to the gravity while the wetting area decreases. It gradually becomes a bulge shape as illustrated in the left panel of Figure 5 and will eventually pinches off (we did not capture the pinch-off phenomenon since the topological change cannot be handled within the current framework). In the hydrophobic case, we set $Bo = 10$ and $\theta_y = 105.75°$. As illustrated in the right panel of Figure 5, the droplet gradually reaches a steady state where the gravity and gradient of pressure balance each other. The steady profile of droplet takes a lightbulb shape with a larger wetting area than that in the hydrophilic case.

Example 4 (Chemical heterogeneity) In this example, we drive the solid substrate with a given velocity U_{pull}. Then the droplet will move relative to the substrate. This is a classical scenario in the coating industry. The CAC (16) and the NBC (13) are modified to be

$$\pm\beta_{cl}^* Ca(u_{cl} - U_{pull}) = \cos\theta_d - \cos\theta_y, \ u - U_{pull} = \lambda l_s \frac{\partial u}{\partial y}.$$

We are interested in the case that there is chemical heterogeneity in the substrate. The chemical pattern is imposed on the substrate by a periodic structure in the Young's angle $\theta_y = \varphi(\frac{\hat{x}_{cl}}{\epsilon})$, where $\hat{x}_{cl} = x_{cl} - U_{pull}t$ is the relative position of the contact line on the substrate, φ is a periodic function with period 1, and ϵ is the period of the chemical roughness. For simplicity,
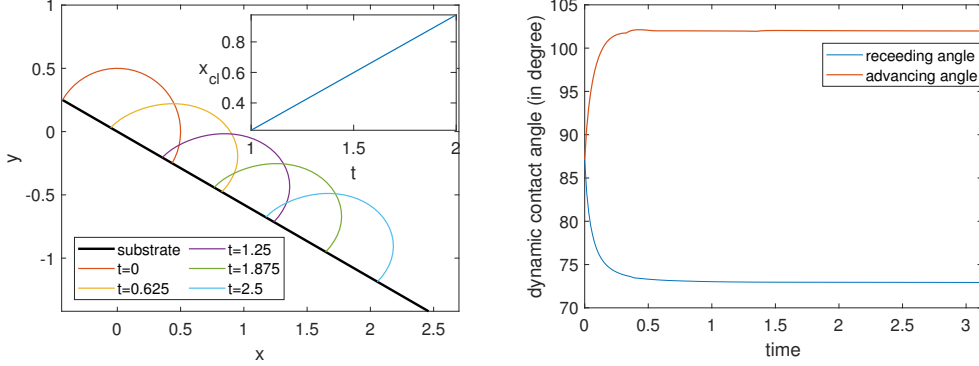
18

Figure 4: Droplet sliding along a slope with $\theta_{slope} = 30°$. Young's angle is $\theta_y = 90°$. The left panel shows the shape of the interface at different time snapshots, while the inset plot shows the constant-speed movement of the contact line after some time. The right panel depicts the dynamics of the advancing and receding angles.
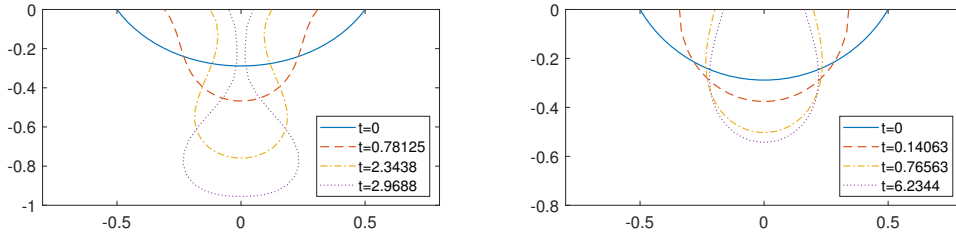

Figure 5: Kelvin pendant droplets: the droplets are elongated by gravity and deform to different shapes. The Bond number and Young's angle are $Bo = 20, \theta_y = 60.75°$ in the left panel and $Bo = 10, \theta_y = 105.75°$ in the right panel.

we choose θ_y to be piecewise constant,

$$\varphi(x) = \left\{ \begin{array}{ll} \theta_y^A, & 0 < x < \frac{1}{2}, \\ \theta_y^B, & \frac{1}{2} < x < 1, \end{array} \right.$$

where $\theta_y^A = 84.27°$, $\theta_y^B = 95.73°$, and $\epsilon = 0.01$.

After the application of a driven velocity $U_{pull} = 1.6$, the droplet moves on the substrate with its head and tail behaving differently and periodically in an alternating manner. At one stage, the head of the droplet (the part of the interface near the left contact line) moves slowly with a slowly varying advancing contact angle, while the tail (the part of the interface near the right contact line) moves fast with a quickly varying receding contact angle

19

(shown in the left panel of Figure 6). At another stage, the head and tail of the droplet behave in an opposite way: the head moves fast while the tail moves slowly. These two stages occur alternatingly and periodically. In the whole process, the droplet moves like "a creeping inchworm" [37]. If we zoom in the interface profile nearby the right contact line (shown in the right panel of Figure 6), we can see that during the period $t \in [1.01, 1.23]$ the interface away from the contact line remains almost unchanged, while the contact line slips very quickly on the substrate at the same time period. When $t \in [1.23, 1.45]$, the contact line moves very slowly as if it gets stuck at some position. The interface gradually adjusts itself and thus the receding angle increases. This is the well known stick-slip phenomenon.
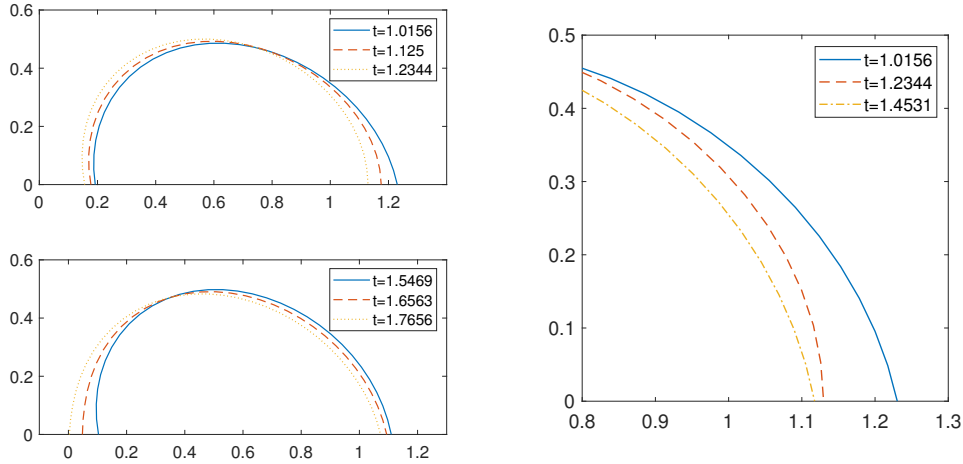
Figure 6: Inchworm movement: $U_{pull} = 1.6$, $\theta_y^A = 80.21°$, $\theta_y^B = 97.40°$. The left panels show a creeping inchworm like moving pattern. The interface profile near the right contact line is zoomed in and shown in the right panel.

We also measure the advancing (left) and receding (right) contact angle, and plot these angles and the contact line displacement in Figure 7. From the left panel, we can clearly see the stick-slip behavior of the left contact line displacement. The stick-slip period is exactly the period of chemical roughness ϵ. This is also confirmed from the dynamics of the receding and advancing contact angles as shown in the right panel. Moreover, the average velocity of the contact line is proportional to U_{pull}, and the advancing and receding contact angles oscillate around their average values $90.50°$ and $77.69°$ respectively. As ϵ turns smaller, the oscillations of the dynamic contact angles

20

around their average values become smaller. It can be expected that the dynamic advancing and receding contact angles converge to their "average" values in the limit of $\epsilon \to 0$, which results in the contact angle hysteresis effect.
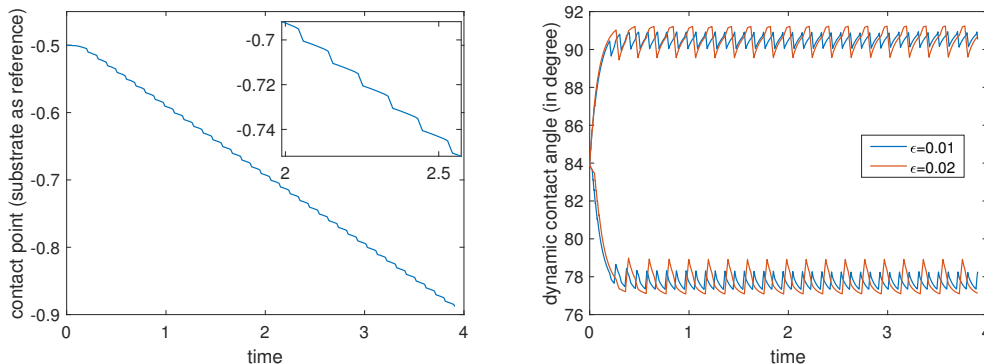

Figure 7: Dynamic plots of the contact line displacement and the contact angle with $U_{pull} = 1$. The Young's angle is piecewise constant $\theta_y^A = 84.27°$ or $\theta_y^B = 95.73°$ with period $\epsilon = 0.01$ (blue line) or $\epsilon = 0.02$ (red line). Left panel: the displacement of the left contact line. Right panel: the dynamic advancing and receding contact angles.

Furthermore, for $\epsilon = 0.1$, $\theta_y^A = 81.41°$, $\theta_y^B = 98.59°$, we vary the values of U_{pull} from 1 to 0.01 and study the dependence of the advancing angle on the driving velocity U_{pull}. As shown in Figure 8. The advancing angle decreases as U_{pull} decreases.

The limiting behavior of the contact line displacement and the contact angles for small roughness limit $\epsilon \to 0$ and their analytical dependence on driving speed U_{pull} go beyond the study of this paper. We will leave its quantitative study to our future work. We also refer readers to [38] for the existing analytical study.

Example 5 (Discontinuous viscosity) In this example, we consider two-phase flows with discontinuous viscosity. The convergence rate are presented in Table 2, where the viscosity ratio is 0.1 : 1 and errors are computed at $t = 1.7578$. We can clearly observe the second order convergence in the velocity field and the contact line, although we cannot show that by truncation error analysis.

We also simulate two-phase flows with different viscosity ratios on the solid substrates. The interface initially stays in a steady profile of semi-circular shape with the Young's angle $\theta_y = 90°$. The substrate is pulled at
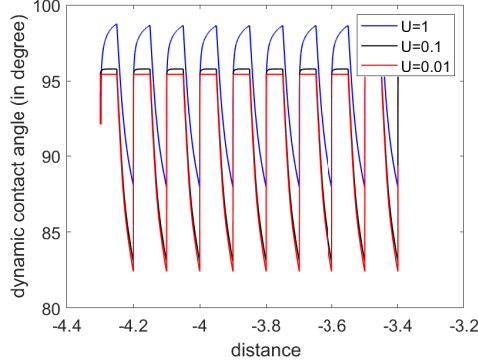
21

Figure 8: Advancing angles with different pulling velocity on a substrate: $\epsilon = 0.1$, $\theta_y^A = 81.41°$, $\theta_y^B = 98.59°$

$N_x \times N_y$	$\|E_u\|_2$	order$_u$	$\|E_{cl}\|_\infty$	order$_{cl}$
32×16	$3.3972e-03$		$1.7716e-02$	
64×32	$9.9172e-04$	1.7764	$4.7247e-03$	1.9067
128×64	$2.6801e-04$	1.8877	$1.2532e-03$	1.9146
256×128	$6.0426e-05$	2.1490	$2.5064e-04$	2.3219

Table 2: Errors and convergence order of velocity fields and contact lines. Absolute errors of velocity field E_u and contact line position E_{cl} are computed by comparing with numerical solution on grids with $N_x \times N_y = 512 \times 256$. $\|\cdot\|_2$ and $\|\cdot\|_\infty$ denote l_2 and l_∞ norms.

the velocity $U_{pull} = 1$. We use different viscosity ratios of $0.1 : 1$, $1 : 1$, and $1 : 0.1$ to simulate three typical scenarios: a droplet in air, two fluids with close viscosity, and a bubble surrounded by water respectively. The interface motions in these three cases become very different eventually. The snapshots of the interfaces at $t = 7.8125$ are shown in Figure 9. Comparing the fluid-fluid interface of equal viscosities (solid red line) with the interface of a droplet in the air (dashed blue line), we observe that the droplet is more easily pulled towards right along with the substrate if it has a larger viscosity than that of the environment. These two interfaces are not deformed too much and are of similar shape. However, in the case that the inside fluid is less viscous than the environmental fluid, like a bubble staying in the water, the bubble is heavily deformed and moves a little bit slowly on the substrate. We can clearly see a large advancing angle on the left contact line and a

22

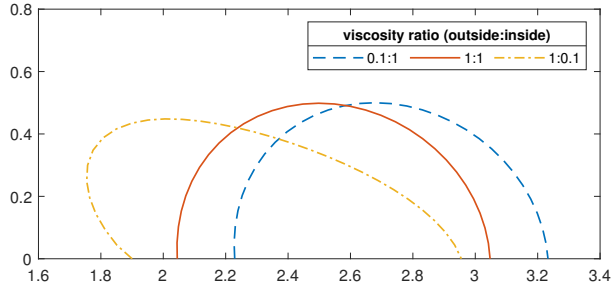small receding angle on the right contact line.

Figure 9: Solid red line: a droplet surrounded by fluid with close viscosity. Dash blue line: a droplet in air. Dash dot yellow line: a bubble in water.

5. Conclusion

In this work, we developed a second order accurate numerical method to simulate moving contact line problems. We considered the two-phase Stokes problem with Navier-slip boundary condition and contact angle condition. Following the framework of immersed interface methods, we derived correction terms at the irregular grid points nearby the interface and obtained a finite difference scheme for the Stokes system. To take care of the irregular points near the contact lines, we choose the closest midpoints on the interfacial line segments as the projection points when deriving correction terms.

In order to keep sufficient accuracy in the correction terms and the truncation errors, we required second order accurate approximations of the interface and its curvature. This was achieved by using a parametric finite element method on the interface. The interface and the contact line position were solved as well as the curvature in a variational framework. After a bilinear interpolation of the velocity field to the interface, the PFEM solver for the interface was coupled with the IIM solver for the velocity field. This yields a second order accurate numerical method for the contact line dynamics as well as the velocity field. Moreover, the algorithm was generalized to deal with the problems with discontinuous viscosity.

The second order accuracy was numerically validated in the benchmark problem of droplet relaxation on a substrate. Numerical simulations of sliding

droplet and Kelvin pendant were investigated. In particular, contact angle hysteresis was numerically studied in the case of chemically heterogeneous surface. The contact line motion was observed to show stick-slip behavior periodically. The advancing and receding contact angles oscillated around their average values, which depended on the pulling velocity of the substrate.

The current study concentrates on the moving contact lines using Stokes model. However, in most realistic situations, the inertial effect cannot be neglected. In the future work, we will generalize our method to solve the contact line dynamics with Navier-Stokes equations. To speed up the computations, we will also investigate the energy stable schemes and develop fast solvers. The asymmetric dependence of the advancing and receding contact angles on the substrate velocity has been studied experimentally in the context of contact angle hysteresis [40]. This interesting phenomenon needs more numerical studies and mathematical analysis, and will be our future concern.

Acknowledgments

Appendix A. Derivations of the jump conditions

The derivations of jump conditions are based on local coordinate systems. A point $\mathbf{X}^*$ on the interface Γ is chosen to be the origin and the normal and tangential directions are the axes as shown in Figure A.10. The local coordinates can be written as

$$
\begin{aligned}
\tilde{x} &= (x - X^*)\cos\psi + (y - Y^*)\sin\psi, \\
\tilde{y} &= -(x - X^*)\sin\psi + (y - Y^*)\cos\psi,
\end{aligned}
$$

where ψ is the angle between the x-axis and the outward normal directions. Therefore in the local coordinate system, any point $\mathbf{Q}$ can be written as

$$
\mathbf{Q} = \mathbf{X}^* + \tilde{x}\mathbf{n} + \tilde{y}\boldsymbol{\tau},
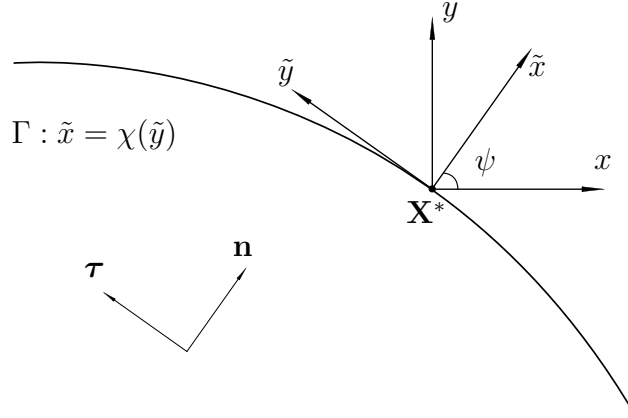$$

24

Figure A.10: The local coordinate system.

and velocity field $\mathbf{u}$ is represented by

$$\mathbf{u} = \tilde{u}\mathbf{n} + \tilde{v}\boldsymbol{\tau}.$$

In this local coordinate system, the interface is parameterized as

$$\Gamma = \left\{ (\tilde{x}, \tilde{y}) = (\chi(\tilde{y}), \tilde{y}) \right\},$$

where $\chi(0) = \chi'(0) = 0$, $\chi''(0) = \kappa$. Define the level set function $\phi(\tilde{x}, \tilde{y}) = \tilde{x} - \chi(\tilde{y})$. Then the interface is represented by the zero level set $\{(\tilde{x}, \tilde{y}) : \phi(\tilde{x}, \tilde{y}) = 0\}$. We can extend the normal and tangential vectors to a neighborhood of the interface. Then the local unit normal and tangential vectors are represented by

$$\tilde{\mathbf{n}} = \frac{1}{\sqrt{1 + (\chi')^2}}(1, -\chi'), \quad \tilde{\boldsymbol{\tau}} = \frac{1}{\sqrt{1 + (\chi')^2}}(\chi', 1).$$

Note that $\tilde{\mathbf{n}} = (1, 0)$ and $\tilde{\boldsymbol{\tau}} = (0, 1)$ at the interfacial point $\mathbf{X}^*$.

After taking the inner products of the Stokes equation (10) with $\tilde{\mathbf{n}}$ on the two sides $\{\phi > 0\}$ and $\{\phi < 0\}$ and calculating their difference at the interface, we obtain the interfacial jump condition

$$\left[\frac{\partial p}{\partial \tilde{x}} \right] = \left[\nu_i \left(\frac{\partial^2 \tilde{u}}{\partial \tilde{x}^2} + \frac{\partial^2 \tilde{u}}{\partial \tilde{y}^2} \right) \right]. \tag{A.1}$$

Next, we want to evaluate the right hand side of (A.1). Since the jump condition (12) is defined on the interface $\Gamma = \{(\chi(\tilde{y}), \tilde{y})\}$, we can take the

25

total derivative w.r.t. $\tilde{y}$ to obtain

$$\frac{\mathrm{d}}{\mathrm{d}\tilde{y}}\left[\tilde{\mathbf{n}}\cdot\nu_i\left(\nabla\tilde{\mathbf{u}}+(\nabla\tilde{\mathbf{u}})^\top\right)\cdot\tilde{\boldsymbol{\tau}}\right]=0.$$

The total derivative of the jump on interface can be computed using the following equality

$$
\begin{aligned}
\frac{\mathrm{d}\omega^+(\chi(\tilde{y}),\tilde{y})}{\mathrm{d}\tilde{y}}\bigg|_{\tilde{y}=0} &= \left(\left(\frac{\partial\omega^+(\tilde{x},\tilde{y})}{\partial\tilde{x}}\right)\chi'(\tilde{y})+\frac{\partial\omega^+(\tilde{x},\tilde{y})}{\partial\tilde{y}}\right)\bigg|_{(0,0)} \\
&= \frac{\partial\omega^+}{\partial\tilde{y}}\bigg|_{(0,0)} = \left(\frac{\partial\omega}{\partial\tilde{y}}\right)^+\bigg|_{(0,0)},
\end{aligned}
\tag{A.2}
$$

where $(\cdot)^+$ denotes the limits at the interface approaching from Ω_2, and the last equality holds if $\omega\in C^1$ and $\frac{\partial\omega}{\partial\tilde{y}}$ is bounded in $\Omega_i(i=1,2)$. Similarly, we have

$$\frac{\mathrm{d}\omega^-}{\mathrm{d}\tilde{y}}\bigg|_{\tilde{y}=0}=\left(\frac{\partial\omega}{\partial\tilde{y}}\right)^-\bigg|_{(0,0)}.\tag{A.3}$$

By taking $\omega=\tilde{\mathbf{n}}\cdot\nu_i\left(\nabla\tilde{\mathbf{u}}+(\nabla\tilde{\mathbf{u}})^\top\right)\cdot\tilde{\boldsymbol{\tau}}$ in (A.2) and (A.3), and using the following equality in $\Omega_i(i=1,2)$

$$
\begin{aligned}
\frac{\partial}{\partial\tilde{y}}\left(\tilde{\mathbf{n}}\cdot\nu_i\left(\nabla\tilde{\mathbf{u}}+(\nabla\tilde{\mathbf{u}})^\top\right)\cdot\tilde{\boldsymbol{\tau}}\right) &= \frac{\partial\tilde{\mathbf{n}}}{\partial\tilde{y}}\cdot\nu_i\left(\nabla\tilde{\mathbf{u}}+(\nabla\tilde{\mathbf{u}})^\top\right)\cdot\tilde{\boldsymbol{\tau}} \\
&+\tilde{\mathbf{n}}\cdot\nu_i\left(\nabla\left(\frac{\partial\tilde{\mathbf{u}}}{\partial\tilde{y}}\right)+\left(\nabla\left(\frac{\partial\tilde{\mathbf{u}}}{\partial\tilde{y}}\right)\right)^\top\right)\cdot\tilde{\boldsymbol{\tau}}+\frac{\partial\tilde{\boldsymbol{\tau}}}{\partial\tilde{y}}\cdot\nu_i\left(\nabla\tilde{\mathbf{u}}+(\nabla\tilde{\mathbf{u}})^\top\right)\cdot\tilde{\mathbf{n}},
\end{aligned}
$$

we have

$$\left[\nu_i\left(\frac{\partial^2\tilde{v}}{\partial\tilde{x}\partial\tilde{y}}-2\kappa\frac{\partial\tilde{v}}{\partial\tilde{y}}+2\kappa\frac{\partial\tilde{u}}{\partial\tilde{x}}+\frac{\partial^2\tilde{u}}{\partial\tilde{y}^2}\right)\right]=0.\tag{A.4}$$

Here we have used $\frac{\partial\tilde{\mathbf{n}}}{\partial\tilde{y}}=-\kappa\tilde{\boldsymbol{\tau}}$ and $\frac{\partial\tilde{\boldsymbol{\tau}}}{\partial\tilde{y}}=\kappa\tilde{\mathbf{n}}$ at the origin $(0,0)$. The incompressibility condition and its $\tilde{x}$-derivative are recast in local coordinates as

$$\frac{\partial\tilde{u}}{\partial\tilde{x}}=-\frac{\partial\tilde{v}}{\partial\tilde{y}},\quad\frac{\partial^2\tilde{u}}{\partial\tilde{x}^2}=-\frac{\partial^2\tilde{v}}{\partial\tilde{x}\partial\tilde{y}}.\tag{A.5}$$

26

Substituting (A.4) and (A.5) into (A.1), we obtain the jump condition across the interface Γ

$$\left[\frac{\partial p}{\partial \tilde{x}}\right] = 2\left[\nu_i \frac{\partial^2 \tilde{u}}{\partial \tilde{y}^2}\right] - 4\kappa \left[\nu_i \frac{\partial \tilde{v}}{\partial \tilde{y}}\right].$$

Since these jump values are evaluated at the the interfacial point $\mathbf{X}^*$, the above equation is equivalent to

$$\left[\frac{\partial p}{\partial n}\right] = 2\left[\nu_i \frac{\partial^2 \mathbf{u}}{\partial s^2} \cdot \mathbf{n}\right] - 4\kappa \left[\nu_i \frac{\partial \mathbf{u}}{\partial s} \cdot \boldsymbol{\tau}\right]. \tag{A.6}$$

Appendix B. Coordinate transformation of jump conditions

The jump terms of x- and y- derivatives are represented using normal and tangential derivatives through local coordinate transformation. For the velocity component $u(x,y)$, its second partial derivative w.r.t. x can be written in terms of the local coordinate as

$$\frac{\partial^2 u}{\partial x^2} = \cos^2 \psi \frac{\partial^2 u}{\partial \tilde{x}^2} - 2\sin\psi\cos\psi \frac{\partial^2 u}{\partial \tilde{y}\partial\tilde{x}} + \sin^2\psi \frac{\partial^2 u}{\partial \tilde{y}^2}.$$

By interchanging the limit $\lim_{\tilde{x}\to 0^\pm}$ with partial derivative $\frac{\partial}{\partial \tilde{y}}$, and taking the difference of the limits at the interface from each side $\Omega_i (i = 1, 2)$, we have

$$\left[\frac{\partial^2 u}{\partial x^2}\right] = \cos^2 \psi \left(\left[\frac{\partial p}{\partial x}\right] - \kappa \left[\frac{\partial u}{\partial n}\right]\right)$$
$$- 2\sin\psi\cos\psi \frac{\partial}{\partial s}\left[\frac{\partial u}{\partial n}\right] + \left(\sin^2\psi - \cos^2\psi\right)\frac{\partial^2}{\partial s^2}[u],$$

where we have used the useful relation [39]

$$\frac{\partial^2 u}{\partial n^2} = \nabla^2 u - \frac{\partial^2 u}{\partial s^2} - \kappa \frac{\partial u}{\partial n},$$

and the Stokes equation (10) in the bulk to replace Δu. By using the jump conditions (21) along the interface, we obtain the jump term $\left[\frac{\partial^2 u}{\partial x^2}\right]$ as in (B.1). Other jump terms occurring in the correction terms could be derived in a similar manner. We list the jump conditions as follows

$$\left[\frac{\partial^2 u}{\partial x^2}\right] = \frac{1}{Ca}\left(-\sin\psi\cos^2\psi \frac{\partial \kappa}{\partial s}\right), \quad \left[\frac{\partial^2 u}{\partial y^2}\right] = \frac{1}{Ca}\left(-\sin^3\psi \frac{\partial \kappa}{\partial s}\right), \tag{B.1}$$

27

$$\left[\frac{\partial^2 u}{\partial x \partial y}\right] = \frac{1}{Ca}\left(-\sin^2 \psi \cos \psi \frac{\partial \kappa}{\partial s}\right), \ \left[\frac{\partial u}{\partial x}\right] = 0, \ \left[\frac{\partial u}{\partial y}\right] = 0, \ [u] = 0, \ \text{(B.2)}$$

$$\left[\frac{\partial^2 v}{\partial x^2}\right] = \frac{1}{Ca}\left(\cos^3 \psi \frac{\partial \kappa}{\partial s}\right), \quad \left[\frac{\partial^2 v}{\partial y^2}\right] = \frac{1}{Ca}\left(\sin^2 \psi \cos \psi \frac{\partial \kappa}{\partial s}\right), \quad \text{(B.3)}$$

$$\left[\frac{\partial^2 v}{\partial x \partial y}\right] = \frac{1}{Ca}\left(\sin \psi \cos^2 \psi \frac{\partial \kappa}{\partial s}\right), \ \left[\frac{\partial v}{\partial x}\right] = 0, \ \left[\frac{\partial v}{\partial y}\right] = 0, \ [v] = 0, \quad \text{(B.4)}$$

$$\left[\frac{\partial p}{\partial x}\right] = \frac{1}{Ca}\left(-\sin \psi \frac{\partial \kappa}{\partial s}\right), \ \left[\frac{\partial p}{\partial y}\right] = \frac{1}{Ca}\left(\cos \psi \frac{\partial \kappa}{\partial s}\right), \ [p] = \frac{\kappa}{Ca}. \quad \text{(B.5)}$$

References

[1] G. Korotcenkov, Handbook of gas sensor materials, Volume 1: Conventional Approaches (2013) Springer.

[2] B-J. De Gans, P. C. Duineveld, U. S. Schubert, Inkjet printing of polymers: state of the art and future developments, Advanced materials 16 (3) (2004) 203–213.

[3] T. Young, III. An essay on the cohesion of fluids, Philosophical transactions of the royal society of London 95 (1805) 65–87.

[4] C. Huh, L. E. Scriven, Hydrodynamic model of steady movement of a solid/liquid/fluid contact line, Journal of colloid and interface science 35 (1) (1971) 85–101.

[5] E. B. Dussan, S. H. Davis, On the motion of a fluid-fluid interface along a solid surface, Journal of Fluid Mechanics 65 (1) (1974) 71–95.

[6] J. Koplik, J. R. Banavar, J. F. Willemsen, Molecular dynamics of Poiseuille flow and moving contact lines, Physical review letters 60 (13) (1988) 1282.

[7] P. A. Thompson, M. O. Robbins, Simulations of contact-line motion: slip and the dynamic contact angle, Physical review letters 63 (7) (1989) 766.

[8] D. M. Anderson, G. B. McFadden, A. A. Wheeler, Diffuse-interface methods in fluid mechanics, Annual review of fluid mechanics 30 (1) (1998) 139–165.

28

[9] D. Jacqmin, Contact-line dynamics of a diffuse fluid interface, Journal of Fluid Mechanics 402 (2000) 57–88.

[10] T. Qian, X.-P. Wang, P. Sheng, Molecular scale contact line hydrodynamics of immiscible flows, Physical Review E 68 (1) (2003) 016306.

[11] E. B. Dussan, On the spreading of liquids on solid surfaces: static and dynamic contact lines, Annual Review of Fluid Mechanics 11 (1) (1979) 371–400.

[12] J. D. van der Waals, The thermodynamic theory of capillarity under the hypothesis of a continuous variation of density, Journal of Statistical Physics 20 (2) (1979) 200–244.

[13] X.-P. Wang, Y.-G. Wang The sharp interface limit of a phase field model for moving contact line problem, Methods and Applications of Analysis 14 (3) (2007) 287–294.

[14] Z. Zhang, S. Xu, W. Ren Derivation of a continuum model and the energy law for moving contact lines with insoluble surfactants, Physics of Fluids 26 (6) (2014) 062103.

[15] W. Ren, W. E, Boundary conditions for the moving contact line problem, Physics of fluids 19 (2) (2007) 022101.

[16] W. Ren, D. Hu, W. E, Continuum models for the contact line problem, Physics of fluids 22 (10) (2010) 102103.

[17] C. Josserand, L. Lemoyne, R. Troeger, S. Zaleski, Droplet impact on a dry surface: triggering the splash with a small obstacle, Journal of fluid mechanics 524 (2005) 47.

[18] M. Renardy, Y. Renardy, J. Li, Numerical simulation of moving contact line problems using a volume-of-fluid method, Journal of Computational Physics 171 (1) (2001) 243–263.

[19] P. D. Spelt, A level-set approach for simulations of flows with multiple moving contact lines with hysteresis, Journal of Computational Physics 207 (2) (2005) 389–404.

[20] J. J. Xu, W. Ren, A level-set method for two-phase flows with moving contact line and insoluble surfactant, Journal of Computational Physics 263 (2014) 71–90.

[21] S. Manservisi, R. Scardovelli, A variational approach to the contact angle dynamics of spreading droplets, Computers & fluids 38 (2) (2009) 406–424.

[22] M. Muradoglu, S. Tasoglu, A front-tracking method for computational modeling of impact and spreading of viscous droplets on solid walls, Computers & Fluids 39 (4) (2010) 615–625.

[23] A. Mayo, The fast solution of Poisson's and the biharmonic equations on irregular regions, SIAM Journal on Numerical Analysis 21 (2) (1984) 285–299.

[24] I. B. Bazhlekov, P. D. Anderson, H. E. Meijer, Numerical investigation of the effect of insoluble surfactants on drop deformation and breakup in simple shear flow, Journal of colloid and interface science 298 (1) (2006) 369–394.

[25] C. S. Peskin, The immersed boundary method, Acta Numerica 11 (2002) 479–517.

[26] R. J. LeVeque, Z. Li, The immersed interface method for elliptic equations with discontinuous coefficients and singular sources, SIAM Journal on Numerical Analysis 31 (4) (1994) 1019–1044.

[27] M.-C. Lai, H.-C. Tseng, A simple implementation of the immersed interface methods for stokes flows with singular forces, Computers & fluids 37 (2) (2008) 99–106.

[28] Z. Li, M.-C. Lai, G. He, H. Zhao, An augmented method for free boundary problems with moving contact lines, Computers & fluids 39 (6) (2010) 1033–1040.

[29] J. W. Barrett, H. Garcke, R. Nürnberg, A parametric finite element method for fourth order geometric evolution equations, Journal of Computational Physics 222 (1) (2007) 441–467.

[30] J. W. Barrett, H. Garcke, R. Nürnberg, On the variational approximation of combined second and fourth order geometric evolution equations, SIAM Journal on Scientific Computing 29 (3) (2007) 1006–1041.

[31] W. Bao, W. Jiang, Y. Wang, Q. Zhao, A parametric finite element method for solid-state dewetting problems with anisotropic surface energies, Journal of Computational Physics 330 (2017) 380–400.

[32] Q. Zhao, W. Ren, An energy-stable finite element method for the simulation of moving contact lines in two-phase flows, Journal of Computational Physics (2020) 109582.

[33] K. Ito, Z. Li, X. Wan, Pressure jump conditions for stokes equations with discontinuous viscosity in 2d and 3d, Methods and applications of analysis 13 (2) (2006) 199–214.

[34] Z. Li, K. Ito, The immersed interface method: numerical solutions of PDEs involving interfaces and irregular domains, SIAM, 2006.

[35] Z. Tan, D.-V. Le, K. M. Lim, B. Khoo, An immersed interface method for the incompressible navier–stokes equations with discontinuous viscosity across the interface, SIAM Journal on Scientific Computing 31 (3) (2009) 1798–1819.

[36] W. Thomson, Capillary attraction, Nature 34 (1886) 270-272.

[37] L. Wang, H.-B. Huang, X.-Y. Lu, Scheme for contact angle and its hysteresis in a multiphase lattice boltzmann method, Physical Review E 87 (1) (2013) 013301.

[38] X. Xu, Y. Zhao, X. Wang, Analysis for contact angle hysteresis on rough surfaces by a phase-field model with a relaxed boundary condition, SIAM Journal on Applied Mathematics 79 (6) (2019) 2551–2568.

[39] J.-J. Xu, H.-K. Zhao, An eulerian formulation for solving partial differential equations along a moving interface, Journal of Scientific Computing 19 (1-3) (2003) 573–594.

[40] D. Guan, Y. J. Wang, E. Charlaix, P. Tong, Asymmetric and speed-dependent capillary force hysteresis and relaxation of a suddenly stopped moving contact line, Physical review letters 116 (6) (2016) 066102.